Interplay of Power-Law correlated Disorder and Long-Range Hopping in One Dimension: Mobility Edges, Criticality, and ML-Based Phase Identification

Mohammad Pouranvari

Department of Physics, Faculty of Basic Sciences,

University of Mazandaran, P. O. Box 47416-95447, Babolsar, Iran

(Dated: November 25, 2025)

We investigate a one-dimensional tight-binding model in which onsite potentials $\{\varepsilon_i\}$ exhibit power-law spatial correlations (with exponent α) and the hopping amplitudes decay as $t_{ij} \sim |i-j|^{-\beta}$. This two-parameter family interpolates continuously between short-range Anderson-like disorder, correlated disorder with conventional hopping, and long-range hopping models with nontrivial delocalization tendencies. Using large-scale exact diagonalization, we construct a comprehensive phase map in the (α, β) plane by combining spectral statistics, density-of-states analysis, and energyresolved localization indicators such as the participation ratio, single-particle entanglement entropy, level-spacing ratio r, and the ratio of the geometric to arithmetic density of states. From these observables we define phase-indicator functions that compactly quantify localization behaviour across the spectrum. Our analysis reveals robust mobility edges and multiple regimes of spectral coexistence between localized, extended, resonant, and critical states. Finite-size scaling, implemented via an explicit smoothness-based cost function, enables extraction of critical exponents and delineation of transition lines across the (α, β) parameter space. To validate and complement these physics-based diagnostics, we employ a supervised autoencoder that learns high-level representations of eigenstate structure directly from raw features and reliably reproduces the phase classification defined by the indicator functions. Together, these approaches provide a coherent and internally consistent picture of the spectral transitions driven by correlated disorder and long-range hopping, establishing a unified framework for characterizing mobility edges in long-range one-dimensional systems.

I. INTRODUCTION

The interplay of disorder and quantum interference in low-dimensional systems is a paradigmatic problem in condensed-matter physics[1-5]. In one dimension, the conventional result is simple and robust: for short-range models with uncorrelated disorder, all single-particle eigenstates are exponentially localized in the thermodynamic limit [6, 7]. Departures from this simple picture arise, however, when one of the basic assumptions is relaxed — for example, when the potential landscape contains long-range correlations [8, 9] or when the kinetic energy is long-ranged [10, 11]. Each of these ingredients alone can produce atypical spectral and transport behaviour in one dimension; when combined the resulting phenomenology becomes rich and — in many respects only partially charted. On one hand, tight-binding models with long-range hopping, where the hopping amplitude between sites i and j decays as a power law $|i-j|^{-\beta}$, can host a localization-delocalization transition even in 1D. For sufficiently slow decay ($\beta \leq 1$), the hopping is non-local enough to overcome the localizing effects of disorder, leading to extended eigenstates. Such models have been instrumental in understanding phenomena ranging from transport in disordered systems to the nature of eigenstates in power-law random banded matrices, which often exhibit multifractal properties at the transition point [12–20].

On the other hand, introducing spatial correlations into the disorder potential can also induce delocalization. Potentials with long-range correlations, such as those generated from fractional Brownian motion, can create extended states and even mobility edges separating localized and delocalized states within the energy spectrum [8, 9]. The intuition is that correlated disorder is "smoother" than white-noise disorder, reducing the effectiveness of random scattering[21–25].

While these two mechanisms for delocalization have been studied extensively in isolation, their interplay remains a rich area of investigation. The central question we address in this work is: What is the fate of localization in a 1D system where both long-range hopping and long-range correlated disorder are present simultaneously? This scenario is not merely of academic interest but is relevant to various physical systems, including trapped ions, Rydberg atoms, and polar molecules, where both interactions and external potentials can exhibit long-range characteristics [17, 26–30].

In this work we consider a family of one-dimensional tight-binding Hamiltonians in which (A) the on-site potentials $\{\varepsilon_i\}$ are constructed by Fourier synthesis with random phases so that the power spectrum scales as $S(k) \propto k^{-\alpha}$; the resulting sequence is mean-subtracted and variance-normalized and is approximately Gaussian for large system size. and (B) the hopping amplitude between sites decays algebraically as $|i-j|^{-\beta}$ with exponent β . This two-parameter family interpolates between several limits of current interest: (i) the shortrange, uncorrelated Anderson limit $(\beta \to \infty, \text{ small } \alpha)$, (ii) models with long-range correlated potentials but nearest-neighbour hopping ($\beta \gtrsim 1$, $\alpha \gg 1$), (iii) longrange-hopping chains that have been argued to admit nontrivial critical behaviour and delocalization tendencies for sufficiently small β , and (iv) long-range-hopping

with strongly correlated disorder with the expectation (at first sight) of having extended states across all spectrum. Physically, the correlated potential models capture situations where the disorder arises from a rough substrate or from long-wavelength structural variations; long-range hopping arises naturally in systems with dipolar or Coulomb-mediated tunnelling or in effective single-band descriptions with nonlocal overlap integrals.

A central question we address is whether, and under what conditions in the (α, β) parameter space, there will be a phase transition between delocalized/localized states for the entire spectrum or more interestingly there will be a single-particle mobility edges — energy-dependent transitions between localized and extended eigenstates appear and remain robust with system size. Mobility edges in one-dimensional deterministic quasiperiodic systems are known (for example, in generalizations of the Aubry-André model), and mobility edges have been reported in various models with correlated disorder or long-range hopping [31]. What remains unsettled is a systematic characterization, using a compact and mutually consistent set of diagnostics, of how correlated disorder and algebraic hopping cooperate or compete to produce energy-selective localization.

To address these questions we use a set of complementary spectral and eigenstate diagnostics. We first analyse level statistics through the spacing distribution P(s) and number variance $\Sigma^2(L)$, which distinguish Poisson (localized) from Wigner–Dyson (extended) behaviour. We then employ energy-resolved probes—the participation ratio, single-particle entanglement entropy, and the auxiliary measures S_{proxy} and the ρ -ratio—to characterize eigenstate structure across the band. Finally, we define four phase-classification functions $f_1 - f_4$, which quantify the fractions of energy bins labelled localized, extended, resonant, or critical, providing a compact summary of spectral mixing for constructing the (α, β) phase diagram.

A central emphasis of this work is that energy-resolved analysis is essential: mobility edges appear throughout broad regions of the (α, β) parameter space, and global (spectrum-averaged) quantities obscure the coexistence of localized and extended states. To quantify transitions we adopt a finite-size scaling ansatz together with a smoothness-based cost function, providing an operational route to extract critical points and scaling exponents directly from finite-size data. As an independent cross-check, and to extract high-level structure from raw eigenstate features, we train a supervised autoencoder whose latent-space representation correlates strongly with the physics-based f-indicators and cleanly resolves localized, extended, resonant, and critical regimes.

Main results of the paper are:

• We show that the combined action of power-law-correlated onsite potentials (tuned by α) and algebraically decaying hopping amplitudes (tuned by β) generates extended regions in the (α, β) parameter space where the spectrum exhibits

clear energy-dependent separation between localized and extended states—i.e., robust mobility edges. These boundaries are identified through multiple complementary indicators, including the participation ratio, single-particle entanglement entropy, r-statistics, the DOS-derived quantity ρ , and level-statistics behaviour interpolating between Poisson and Wigner–Dyson limits. Across the full spectrum, we resolve four distinct spectral sectors—localized, extended, resonant, and critical—each associated with well-defined patterns in these observables.

- We introduce four phase-characterization functions f_1, \ldots, f_4 , each constructed from physically interpretable combinations of PR, EE, level statistics, and DOS-related indicators. Each f_i evaluates the number of spectral bins exhibiting localized, extended, resonant, or critical phenomenology, providing an operational classification framework that compresses the high-dimensional diagnostic data into compact, robust phase maps.
- By implementing a finite-size scaling collapse governed by a smoothness-adaptive cost function, we extract transition points and effective scaling exponents for representative cuts through the (α, β) plane. Where the collapse is stable, the inferred critical behaviour is consistent across independent diagnostics, providing a cross-validated characterization of the mobility-edge transitions.
- A supervised autoencoder trained on the windowresolved diagnostic vectors reproduces, with high fidelity, the phase labels obtained from the physicsinformed f-functions. The latent coordinate learned by the model serves as a smooth, interpretable parameter that tracks localized, extended, resonant, and critical behaviour, and thereby offers an independent machine-learning confirmation of the phase structure.

This paper is organised as follows. Section II introduces the model, detailing the construction of power-law correlated onsite potentials and the implementation of algebraically decaying long-range hopping together with the required finite-size normalization. Section III defines all diagnostic tools used throughout the work, including level-statistics measures, participation ratios, multifractal dimensions, entanglement-based indicators, the ρ -ratio, the finite-size scaling ansatz, and the machinelearning pipeline. Section IV presents the main numerical results: level-statistics behaviour, evidence for mobility edges, classification maps, and representative local diagnostics illustrating the coexistence of localized, extended, resonant, and critical states across the spectrum. Finally, Section V summarizes the key findings and outlines several open directions for future research.

II. MODEL

We study a single-band tight-binding model on a one-dimensional chain of length N with open boundary conditions. The Hamiltonian is

$$H = \sum_{i=1}^{N} \varepsilon_i c_i^{\dagger} c_i - \sum_{i \neq j} t_{ij} \left(c_i^{\dagger} c_j + \text{h.c.} \right), \tag{1}$$

where c_i^{\dagger} (c_i) creates (annihilates) a spinless fermion on site i. The onsite potentials $\{\varepsilon_i\}$ are drawn from a Gaussian ensemble with prescribed power-law spatial correlations (see Sec. II A) and the hopping amplitudes t_{ij} decay algebraically with the intersite separation (Sec. II B).

A. Power-law correlated onsite potentials

We generate real onsite potentials by superposing Fourier modes with power-law amplitudes,

$$\varepsilon_j = C_N \sum_{k=1}^{N/2} k^{-\alpha/2} \cos(2\pi j k/N + \phi_k), \qquad (2)$$

where the phases ϕ_k are independent random variables uniformly distributed on $[0, 2\pi)$,

$$\phi_k \sim \mathcal{U}[0, 2\pi),$$

ensuring that each realization is real-valued and statistically translation invariant. The prefactor C_N fixes the finite-N normalization of the spectrum (e.g. $C_N = (2\pi/N)^{(1-\alpha)/2}$), and each realization is shifted and rescaled to have zero mean and unit variance,

$$\varepsilon_j \mapsto \frac{\varepsilon_j - \langle \varepsilon \rangle}{\sqrt{\langle \varepsilon^2 \rangle}}.$$

This construction yields onsite correlations that decay asymptotically as

$$\langle \varepsilon_i \varepsilon_{i+r} \rangle \sim r^{-(2\alpha-1)},$$

so the exponent α tunes the smoothness of the potential: larger α produces longer-range correlations, while smaller α approaches uncorrelated disorder. All onsite potentials used in this work were generated using Eq. (2) (see Figure 1)

B. Algebraic long-range hopping and finite-size normalization

The matrix elements of the kinetic term are taken to decay algebraically with distance,

$$t_{ij} = \frac{t_0}{\mathcal{N}_N(\beta)} \frac{1}{|i-j|^{\beta}}, \qquad i \neq j,$$
 (3)

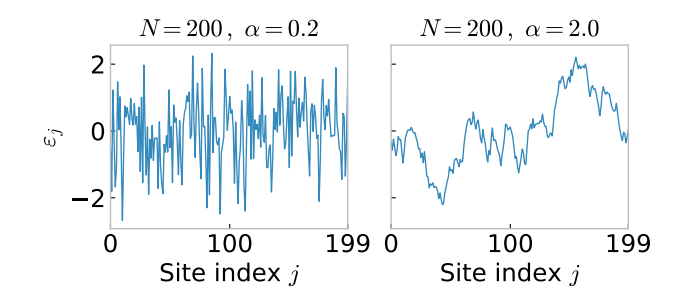


FIG. 1. Real-space onsite potentials ε_j for a chain of length N=200, obtained by superposing Fourier modes with power-law amplitudes [Eq. (2)]. (Left panel) $\alpha=0.2$: weakly correlated, rapidly varying (rough) disorder. (Right panel) $\alpha=2$: enhanced low-k weight produces a much smoother, long-range correlated potential. These representative values illustrate the crossover from rough, short-range disorder at small α to smooth, long-range-correlated landscapes at large α .

where $\beta > 0$ is the hopping-decay exponent. t_0 sets an overall energy scale (we set $t_0 \equiv 1$ in all numerical data shown). To ensure a well-defined thermodynamic limit and maintain the extensivity of the kinetic energy, the hopping term is normalized by a system-size-dependent factor $\mathcal{N}_N(\beta)$ [26, 32]. This normalization factor is chosen as:

$$\mathcal{N}_{N}(\beta) = \begin{cases} \frac{2^{\beta-1}}{1-\beta} N^{1-\beta} & \text{for } \beta < 1, \\ \log N & \text{for } \beta = 1, \\ \zeta(\beta) & \text{for } \beta > 1, \end{cases}$$

where $\zeta(\beta)$ is the Riemann zeta function. In our numerical calculations for $\beta>1$, we approximate $\zeta(\beta)\approx 1/(\beta-1)+\gamma$, where $\gamma\approx 0.5772$ is the Euler–Mascheroni constant.

III. OBSERVABLES AND DIAGNOSTICS

To characterize the different phases of the model, we employ several well-established numerical diagnostics. All spectral and eigenstate-based diagnostics in this work are obtained by exact diagonalization of the single-particle Hamiltonian (Eq.1) for a set of system sizes N (see figure captions for the specific sizes and number of disorder realizations used for each panel). For energy-resolved quantities we typically group eigenstates into energy windows (bins) and report averages and variances across disorder realizations within a chosen window. All of these are computed per eigenstate and then averaged (or aggregated) in energy windows as needed.

A. Level Statistics.

The statistical properties of the energy eigenvalues provide a powerful probe of localization. We analyze the distribution of adjacent level spacings, $s_n = E_{n+1} - E_n$,

after an unfolding procedure to ensure a uniform mean level density. For localized states, the eigenvalues are uncorrelated, leading to a Poisson distribution, $P(s) = e^{-s}$. For delocalized, chaotic states described by random matrix theory, level repulsion leads to a Wigner-Dyson (GOE) distribution, $P(s) = (\pi s/2)e^{-\pi s^2/4}$. We also compute the average ratio of adjacent level spacings, $\langle r_n \rangle = \langle \min(s_n, s_{n-1}) / \max(s_n, s_{n-1}) \rangle$, which avoids the need for unfolding. Its value distinguishes between the Poisson limit ($\langle r_n \rangle \approx 0.386$) and the GOE limit ($\langle r_n \rangle \approx 0.531$) [33].

From the spacings we form the normalized spacing distribution P(s) with $s \equiv \delta/\langle \delta \rangle$ and the (ensemble-averaged) number variance

$$\Sigma^{2}(L) = \langle (N_{L} - \langle N_{L} \rangle)^{2} \rangle, \tag{4}$$

where N_L is the number of eigenvalues in an interval of length L (in unfolded units) and the averages are taken over spectral location and disorder realizations.

B. Participation ratio

For a normalized single-particle eigenstate $\psi_n(i)$ (with eigenstate index n), the participation ratio is defined as

$$PR_n = \frac{1}{\sum_{i=1}^{N} |\psi_n(i)|^4},$$
 (5)

and serves as a measure of the number of sites that significantly contribute to the eigenstate. In the thermodynamic limit, localized states exhibit $PR_n = \mathcal{O}(1)$, whereas fully extended states scale as $PR_n = \mathcal{O}(N)$.

For convenience, we also consider the normalized participation ratio PR_n/N , which vanishes in the localized regime and approaches unity for delocalized states.

C. Generalized multifractal dimensions D(q)

To probe possible multifractality of single-particle eigenstates, we compute the generalized participation moments

$$P_q(n) = \sum_{i=1}^{N} |\psi_n(i)|^{2q}, \tag{6}$$

from which the multifractal exponents are defined via the standard scaling relation

$$D_q(n) = -\frac{1}{(q-1)\log N} \log P_q(n).$$
 (7)

In the thermodynamic limit, localized states yield $D_q \rightarrow 0$, whereas fully extended states satisfy $D_q \rightarrow 1$ for all q. Intermediate values $0 < D_q < 1$ signal multifractal (critical) eigenstates. Throughout this work we evaluate D_q for a discrete set of q values to identify critical spectral windows and to supplement the other localization diagnostics.

D. Entanglement entropy

To characterize the spatial structure of single-particle eigenstates, we employ two entanglement-based diagnostics.

a. (i) Single-particle entanglement entropy. Here the entanglement entropy (EE) is defined for single-particle wavefunctions and should not be confused with the entanglement of many-body eigenstates. For a normalized single-particle state

$$|\psi\rangle = \sum_{i=1}^{N} \psi_i |1_i\rangle, \qquad (8)$$

we bipartition the system into two equal halves, A and B. The probability of finding the particle in subsystem A is

$$p_A = \sum_{i \in A} |\psi_i|^2, \qquad p_B = 1 - p_A.$$
 (9)

Tracing out subsystem B yields a reduced density matrix of rank 2,

$$\rho_A = p_A |1_A\rangle \langle 1_A| + p_B |0_A\rangle \langle 0_A|, \qquad (10)$$

from which the single-particle entanglement entropy is obtained:

$$EE = -(p_A \ln p_A + p_B \ln p_B).$$
 (11)

This entropy is maximal for extended states, where $p_A \approx p_B \approx 1/2$, and is strongly suppressed for localized eigenstates, for which p_A is typically close to either 0 or 1.

b. (ii) Entanglement proxy (sproxy). We define the one-sided Shannon-type proxy

$$s_{\text{proxy}}^{(n)} = -\sum_{i \in A} w_i^{(n)} \ln w_i^{(n)}, \qquad w_i^{(n)} = |\psi_n(i)|^2, \quad (12)$$

which measures how the probability weight is distributed within subsystem A. Unlike the single-particle EE, which depends only on the total weights p_A and p_B and can therefore be large for a state localized near the bipartition (when $p_A \approx p_B \approx 1/2$), $s_{\rm proxy}$ is small whenever the amplitude in A is concentrated on a few sites. Consequently, comparing EE and $s_{\rm proxy}$ allows us to distinguish truly extended states (both EE and $s_{\rm proxy}$ large) from localized states whose support happens to straddle the cut (large EE but small $s_{\rm proxy}$).

E. ρ -ratio

To quantify the degree of spectral mixing within a fixed energy window, we employ the ρ -ratio, a spectral diagnostic constructed directly from the local density of states (LDOS). For an eigenenergy E_n we define the LDOS at site i as $\rho_i(E_n) = |\psi_n(i)|^2$. From this object we construct

two coarse-grained spectral measures evaluated within a given energy bin: the *average* LDOS

$$\rho_{\text{avg}} = \frac{1}{N_{\text{counted}}} \sum_{i} \rho_i(E_n) \tag{13}$$

and the typical LDOS,

$$\rho_{\text{typ}} = \exp\left[\frac{1}{N_{\text{counted}}} \sum_{i} \ln(\rho_i(E_n))\right]. \tag{14}$$

The ρ -ratio is then defined as

$$R_{\rho} = \frac{\rho_{\text{typ}}}{\rho_{\text{avg}}}.$$
 (15)

This quantity behaves analogously to the conventional IPR/IPR_{typ} ratio: it is close to unity when LDOS values are narrowly distributed (as in extended or ergodic regimes) and strongly suppressed when the distribution is broad or log-normal (as in localized regimes).

All observables above can be made energy-resolved by averaging over eigenstates whose energies fall within a chosen energy bin centered at E. Mobility edges (energy-dependent transitions between localized and extended states) are identified by consistent changes in multiple energy-resolved observables.

F. Finite-size scaling ansatz and cost function

To quantify transitions we adopt the finite-size scaling ansatz used in the source material,

$$\frac{F(N,t)}{N^{\gamma_1}} = \mathcal{F}(N^{\gamma_2}(t-t_c)), \tag{16}$$

where F(N,t) is a suitably chosen observable (for instance a chosen f_i), t is the tuning parameter (e.g., β or α), and $(t_c, \gamma_1, \gamma_2)$ are the critical parameters to be optimized. In practice we discretize t on a grid and seek the values of t_c, γ_1, γ_2 that minimize a cost function that measures deviations from a single, smooth scaling curve across system sizes.

The cost function used in the paper is a smoothness regularizer that penalizes spurious oscillatory structure. The smoothness cost used in constructing classification maps is

$$C = \frac{\sum_{i=1}^{N_p - 1} |Q_{i+1} - Q_i|}{\max_i Q_i - \min_i Q_i} - 1, \tag{17}$$

where $\{Q_i\}_{i=1}^{N_p}$ is the sequence of diagnostic values (for example, a monotonic sequence of f-values) sampled along a path in parameter space. minimization proceeds with standard nonlinear optimization routines over the three parameters $(t_c, \gamma_1, \gamma_2)$.

G. Machine-learning pipeline

To complement physics-based indicators we employ a supervised autoencoder (SAE) architecture that combines representation learning with a classification head. The SAE is trained on per-eigenstate (or per-energy-window) feature vectors built from a subset of the observables introduced above. The model consists of an encoder that maps the input feature vector to a low-dimensional latent representation, a decoder that reconstructs the input, and a small classifier head attached to the latent representation that predicts class labels (localized / extended / mixed / critical) derived from the f_i indicators. The SAE is trained with a composite loss

$$\mathcal{L} = \mathcal{L}_{rec} + \mu \mathcal{L}_{class}, \tag{18}$$

where \mathcal{L}_{rec} is a reconstruction loss (mean-squared error) and $\mathcal{L}_{\text{class}}$ is a cross-entropy classification loss; μ balances the two objectives. Training proceeds by stochastic gradient descent (or Adam-type optimizers) on a randomly shuffled dataset; a validation subset is held out to monitor overfitting and to choose early stopping. The SAE both reproduces the physics-based labels and yields a low-dimensional latent coordinate that correlates with the continuous f_i indicators.

H. Implementation notes and reproducibility.

All numerical spectra were generated using a custom C++ exact-diagonalization code employing standard LAPACK routines for dense eigensolvers. For each pair of parameters (α,β) we diagonalized systems up to N=1024 sites and accumulated multiple disorder realizations (the precise number of realizations used for each figure is stated in its caption). Raw eigenvalues and eigenvectors were stored in text form and subsequently parsed and analyzed using Python.

Energy-resolved observables (PR, single-particle entanglement entropy, $s_{\rm proxy},$ and the density-of-states quantities used for $\rho_{\rm typ}$ and $\rho_{\rm ave})$ were evaluated on the full spectrum, then coarse-grained within energy windows of width W=2 and binned using $N'_{\rm bin}=40$ bins unless stated otherwise. For windowing-based analyses, realizations that did not contain sufficient levels inside the window were automatically discarded. All global (spectrum- averaged) quantities were computed only after disorder averaging across the surviving realizations.

Level-spacing distributions and number-variance data were computed after standard unfolding using polynomial fits of the integrated density of states. All finite-size—scaling collapses were performed using the explicit cost function described in Sec. II, with systematic variation of collapse windows and smoothness penalties to monitor stability.

The supervised autoencoder was trained on per- (α, β) feature vectors containing the coarse-grained values of

 $\{r, \rho_{\rm typ}/\rho_{\rm ave}, PR_{\rm norm}, s_{\rm proxy}\}$ across all bins. Training used an 80/20 split, early-stopping with patience of 5 epochs, and a fixed latent dimension of four to match the number of physics-based f-indicators. All ML analyses were performed on CPU in standard PyTorch without GPU acceleration.

IV. RESULTS

In this section, we first study the general picture we can obtain from the adjacent level distribution. Then we look into the entire spectm

A. Level statistics: spacing distribution and number variance

To elucidate the nature of eigenstate statistics and spectral correlations, we compute the level spacing distribution P(s) and the number variance $\Sigma^2(L)$ for various representative points in the (α,β) parameter space. All data is obtained from spectra unfolded via local polynomial fitting, averaged over multiple disorder realizations. We compare the numerically obtained P(s) and $\Sigma^2(L)$ against several theoretical benchmarks: the Poisson distribution, the Wigner-Dyson (WD) distribution, the semi-Poisson form, and the Brody distribution parameterized by the interpolation exponent b.

Figure 2 presents four representative cases corresponding to the corners of the parameter space: $(\alpha, \beta) = (0.5, 0.5)$, (0.5, 3.5), (3.5, 0.5), and (3.5, 3.5). These selections are indicative of regimes with weak and strong correlations in both short and long range hopping.

In the weak-correlation, long-range hopping regime ($\alpha=0.5,\ \beta=0.5$), the level–spacing distribution exhibits a pronounced deviation from the Wigner–Dyson form and falls between the semi–Poisson and Brody distributions (with a fitted Brody parameter $b\approx0.23$), signaling intermediate spectral statistics. For the same interaction exponent α but with strongly decaying hopping amplitudes ($\beta=3.5$), the resulting spectrum again lies in neither the Poisson nor the Wigner–Dyson limits, further confirming the presence of intermediate statistics in this regime.

At high disorder correlation ($\alpha=3.5$) we see similar intermediate behavior. For long-range hopping ($\beta=0.5$), the spacing distribution again indicates intermediate statistics, with a fitted Brody parameter $b\approx0.55$. However, when both disorder correlation and hopping decay are strong ($\beta=3.5$), the level repulsion becomes pronounced, with P(s) exhibiting a sharp peak and suppressed small-s behavior. This regime approaches the Wigner-Dyson limit ($\beta\approx1$), suggesting a delocalized phase with strong level repulsion.

The number variance $\Sigma^2(L)$, shown as insets in each panel, further supports these conclusions. For the parameter sets $(\alpha, \beta) = (0.5, 0.5)$ and (0.5, 3.5), $\Sigma^2(L)$ remains

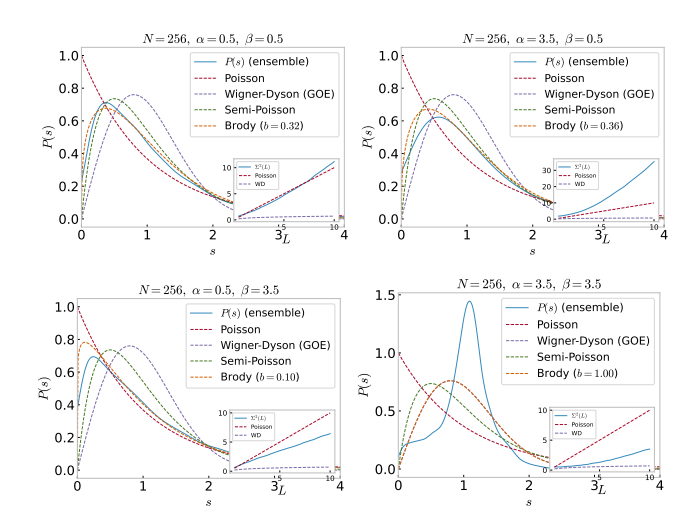


FIG. 2. Level—spacing distributions P(s) and number variances $\Sigma^2(L)$ are shown for four corner points in the (α, β) parameter space at system size N=256. Each panel compares the numerical spacing distribution with standard theoretical benchmarks: Poisson, Wigner–Dyson (WD), semi–Poisson, and Brody forms. The insets display $\Sigma^2(L)$, which further substantiates the evolution from localized to delocalized spectral statistics as functions of the disorder–correlation exponent α and the hopping–range exponent β . For each parameter set, the results are averaged over 200 disorder realizations.

closer to the Poisson prediction (albeit with deviations). In contrast, for the other two parameter combinations, the behavior of $\Sigma^2(L)$ departs from both Poisson and Wigner–Dyson limits, indicating a distinct form of spectral rigidity.

B. Mobility Edge Signatures from Energy-Resolved Observables

To identify possible mobility edges—transitions between localized and extended states within the energy spectrum—we examine energy-resolved diagnostics at representative points in the (α, β) parameter space. Specifically, we analyze the behavior of the participation ratio $\langle PR \rangle$ and the multifractal dimension $\langle D_q \rangle$ as functions of the Fermi energy E_F . Figure 3 presents these quantities for four selected parameter sets: $(\alpha, \beta) = (0.5, 0.5), (0.5, 3.5), (3.5, 0.5),$ and (3.5, 3.5). In all cases, a clear energy dependence emerges. This behavior supports the existence of a mobility edge, separating a delocalized region from localized states.

Having established in Sec. IV A that the global level-spacing distribution neither conforms to pure Poisson statistics (nominally localized) nor to a clean Wigner–Dyson form (nominally extended), and having shown in Sec. IV B that energy-resolved indicators reveal well-defined mobility edges, it becomes essential to inspect the full spectrum using a broader set of local diagnostics. In particular, we examine the normalized participation ra-

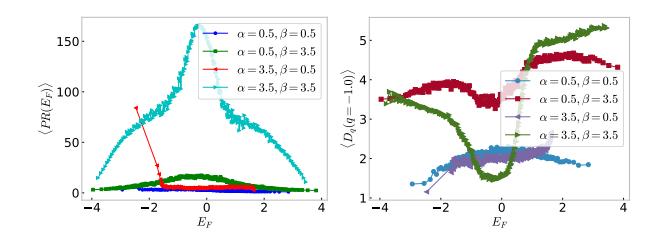


FIG. 3. Energy-resolved behavior of (left) average participation ratio $\langle PR \rangle$ and (right) multifractal dimension $\langle D_q \rangle$ for selected (α, β) pairs.

tio PR/N, the single-particle entanglement entropy, the smoothness indicator $s_{\rm proxy}$, the ratio $\rho_{\rm typ}/\rho_{\rm ave}$, and the spectral ratio r (see Figure 4). These quantities—each sensitive to distinct aspects of localization, spatial structure, and spectral regularity—jointly illuminate how different classes of eigenstates (localized, extended, resonant, and critical) coexist and reorganize across the band (see below for exact definitions).

C. Classification maps and local diagnostics

We summarize the parameter-dependent localization behavior using energy–parameter classification maps, which assign each narrow energy bin one of four labels (localized, resonant, critical/multifractal, extended) based on a multi-metric criterion. The classifier operates on ensemble-averaged quantities computed in narrow energy bins: the spectral-spacing ratio r (Poisson $\langle r \rangle \approx 0.386$, GOE $\langle r \rangle \approx 0.531$), the typical-to-arithmetic DOS ratio $\rho_{\rm typ}/\rho_{\rm ave}$, the normalized participation ratio PR/N, and a spectral-clustering proxy (s_{proxy}) . We use the conservative thresholds

$$r_{\text{low}} = 0.42,$$
 $r_{\text{high}} = 0.50,$ $\rho_{\text{lo}} = 0.15,$ $\rho_{\text{hi}} = 0.60,$ $PR_{\text{lo}} = 0.05,$ $PR_{\text{hi}} = 0.30,$ sproxy_{th} = 0.35. (19)

Bins are labeled extended only when all spectral, density-of-states, and eigenstate–structure indicators consistently signal delocalization—namely, when the spacing ratio r approaches the GOE value, the typical DOS is comparable to the arithmetic DOS ($\rho_{\rm typ}/\rho_{\rm ave} \sim 1$), and the participation ratio is appreciable (PR/N above threshold), indicating wavefunctions spread over a finite fraction of the system. Conversely, a bin is labeled localized when these same diagnostics all fall below their low thresholds: Poisson-like r, strongly suppressed $\rho_{\rm typ}$, and small PR/N, together reflecting exponentially localized eigenstates with sparse spectral support.

We identify resonant bins as those in which eigenstates display large participation ratios yet retain localized spectral character—specifically, where PR/N is elevated but $\rho_{\rm typ}/\rho_{\rm ave}$ remains small or the clustering proxy

(sproxy) indicates poor hybridization across sites. Such states arise when a few spatially proximate sites hybridize strongly, producing locally extended (clustered) amplitudes without generating global ergodicity.

All remaining bins, where different diagnostics point in different directions (e.g., moderately enhanced r, partial suppression of $\rho_{\rm typ}$, or intermediate ${\rm PR}/N$), are labeled critical/multifractal. These reflect states that are neither localized nor fully extended, but display scale-dependent spreading characteristic of critical or multifractal wavefunctions.

Main observations. Across sweeps in either α or β , we observe a robust sequence: predominantly localized spectra for $\alpha, \beta < 1$; the emergence of critical regions near the band center for $1 \leq \alpha, \beta \leq 2$; and nucleation of extended states at the band center for $\alpha, \beta > 2$, expanding outward with increasing hybridization. Resonant pockets appear in regimes where PR/N is large but $\rho_{\rm typ}/\rho_{\rm ave}$ and r remain localized-like, highlighting the limitation of single-metric interpretations.

D. State-fraction maps in the α - β plane

Figure 6 presents the state-weighted fractions $f_{\rm ext}$, $f_{\rm loc}$, $f_{\rm res}$ and $f_{\rm crit}$ (panels: extended, localized, resonant, critical, respectively) computed for N=256. For each parameter pair (α,β) we subdivide the spectrum into $n_{\rm bins}=100$ energy bins , classify each bin using the composite decision tree described in Sec. IV C and form state-weighted fractions by summing bin occupancies (counts) per class and normalizing by the total occupied states for that key. The maps therefore report the fraction of spectral weight assigned to each phenomenological class, averaged over disorder realizations (counts-weighted averaging).

The most salient, reproducible feature is a robust delocalized pocket in the upper-right region of parameter space: states become progressively more extended as both correlation strength (α) and the effective shortrange normalization parameter (β) increase (upper-right quadrant). Conversely, the lower-left region (small α or small β) is dominated by localized character. Resonant bins accumulate adjacent to the extended pocket (consistent with large spatial weight but incomplete spectral rigidity), while the critical fraction outlines a curved transition collar that interpolates between localized and extended regimes. These patterns are qualitatively consistent with the energy-resolved diagnostics shown in Fig. 4

Interpretation and caveats: the maps indicate a smooth crossover surface in (α, β) that separates Poisson-like and GOE-like behavior; however, finite-size effects, the energy dependence of the density of states, and the particular threshold choices in the classifier can shift apparent boundaries. To convert the observed crossover into a bona fide phase transition we must perform finite-size scaling of $f_{\rm ext}$ and $f_{\rm crit}$ along representative cuts, to fol-

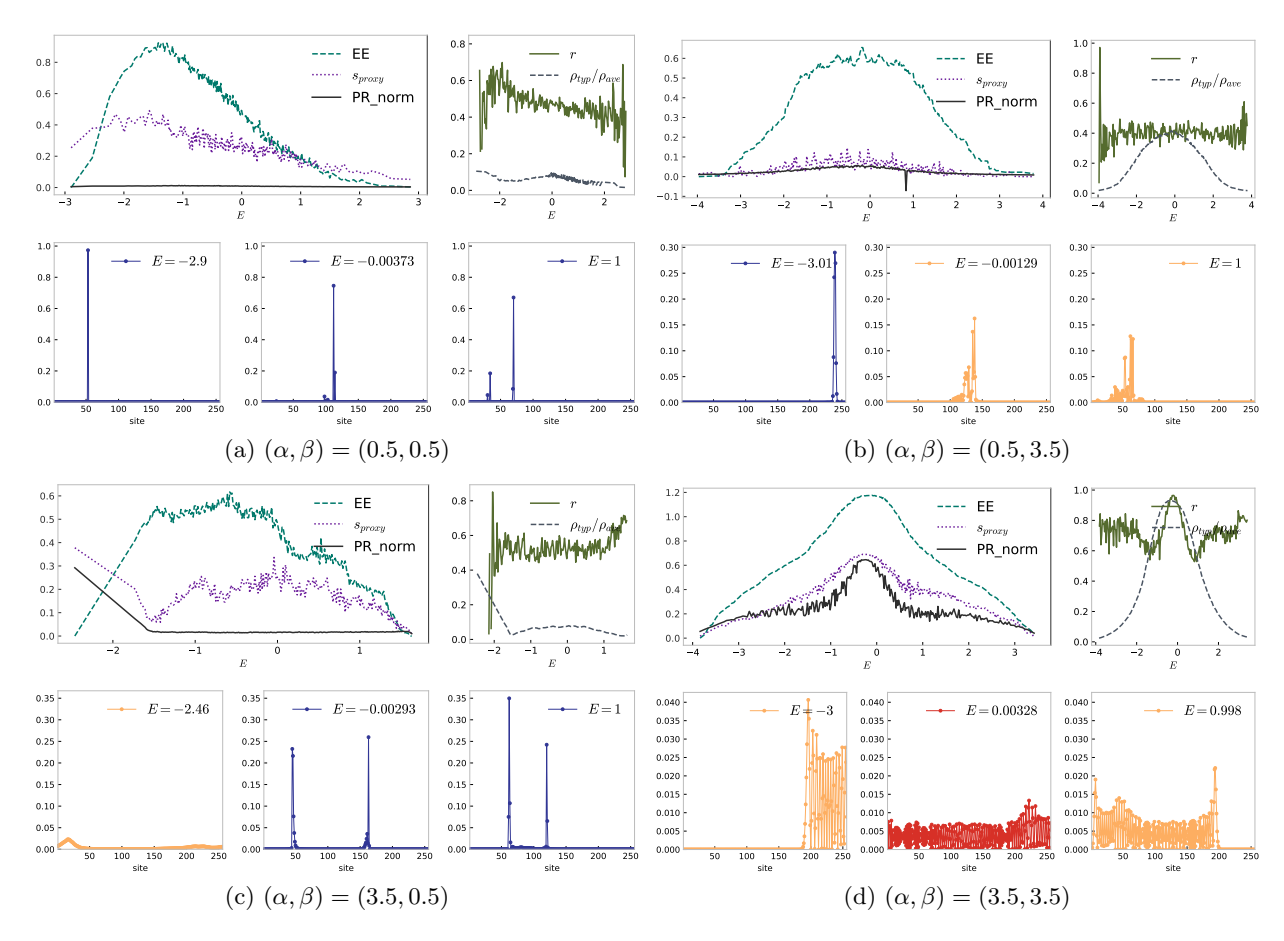


FIG. 4. Composite local diagnostics for representative parameter points. Each panel contains: Top-left: the normalized participation ratio PR/N, plotted together with the single-particle entanglement entropy and $s_{\rm proxy}$, each resolved by energy. Top-right: the binned spectral ratio r and the density-of-states ratio $\rho_{\rm typ}/\rho_{\rm ave}$, both highlighting spectral regions that deviate sharply from the expected localized or extended limits. Bottom row: three representative eigenstate intensities $|\psi(i)|^2$ taken from energies near the band center, mid-band, and band edge. Each intensity profile is colored according to the classifier label associated with its energy bin (color scheme consistent with Fig. 5).

low.

E. Finite-size scaling analysis

We perform finite-size scaling analyses to extract the critical parameters associated with the transitions observed in the state-class fractions f (localized, resonant, critical, extended). For a chosen observable f (one of the four state-fractions) and for a one-dimensional control parameter t (either β for fixed α sweeps or α for fixed β sweeps), we adopt the standard two-parameter scaling ansatz Eq. 16 with t_c is the critical point, γ_1 and γ_2 are finite-size scaling exponents, and \mathcal{F} is an unknown, smooth scaling function (see Sec. IIIF). Successful data collapse (i.e., a single curve for several N when plotted versus the scaling variable $N^{\gamma_2}(t-t_c)$) is taken as numerical evidence for a continuous transition described by the ansatz above.

To determine the optimal collapse parameters $(t_c, \gamma_1, \gamma_2)$, we employ an automated numerical proce-

dure based on minimizing the collapse cost function. For each class $c \in \{\text{localized, resonant, critical, extended}\}$ and for each sweep mode (fixed α or fixed β), we generate the corresponding data sets f(N,t) for system sizes $N = \{128, 256, 384, 512\}$ over a dense grid of the tuning parameter t. Figure 7 displays the extracted critical points in the (α, β) plane. The resulting critical points show excellent consistency with the boundaries inferred from Fig. 6.

To illustrate typical collapse quality, Fig. 8 presents four representative collapse panels. Each subplot shows several system sizes N, the rescaled abscissa $N^{\gamma_2}(t-t_c)$, and the rescaled ordinate f/N^{γ_1} . The legend block lists the optimized parameters $(t_c, \gamma_1, \gamma_2)$ obtained for that fixed value.

A representative set of extracted critical exponents is shown in Fig. 9. Although one might naively expect universal exponent values across different transition lines, our data do not support such a scenario within the accessible system sizes. Instead, we find that the effective exponents γ_1 and γ_2 fall within narrow and well-separated

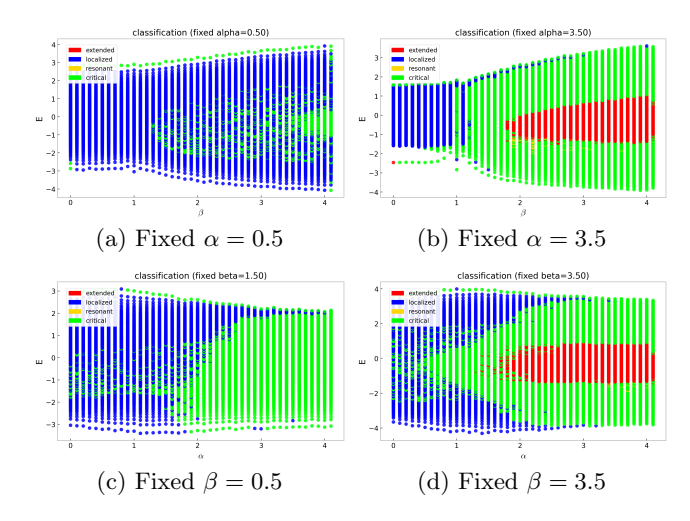


FIG. 5. Classification maps in the energy–parameter plane. Each panel shows the classifier output at N=256, averaged over ~ 200 disorder realizations. Color code: blue = localized, yellow = resonant, green = critical/multifractal, red = extended.

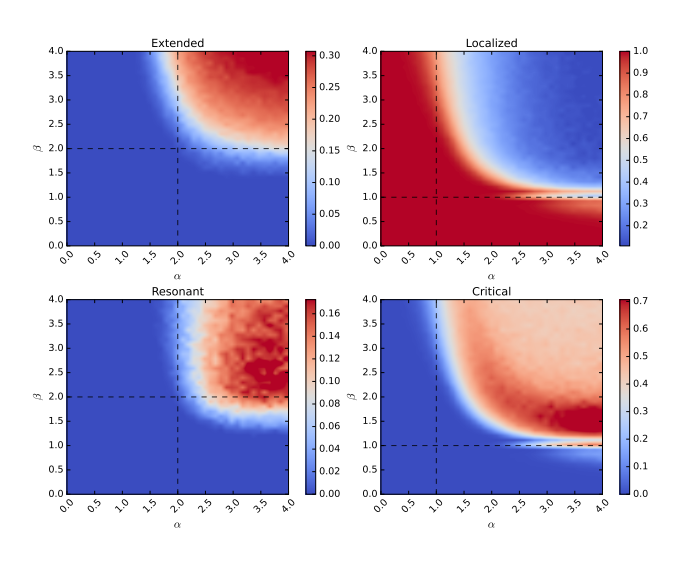


FIG. 6. State-weighted fraction maps for N=512. Each panel shows the fraction f of spectral weight classified as (top-left) extended, (top-right) localized, (bottom-left) resonant, and (bottom-right) critical. For each (α,β) the spectrum is binned $(n_{\rm bins}=100)$ and bins are classified using the composite thresholds on r, $\rho_{\rm ratio}$ and PR_{norm} described in Sec. IV C; fractions are counts-weighted and disorder-averaged.

ranges: for all reliably collapsing cases $\gamma_1 < 0.3$ and $\gamma_2 < 0.5$. The broad spread in fitted values likely reflects (i) pronounced finite-size effects inherent to power-law hopping and correlated disorder, (ii) the non-universality expected in systems with mobility edges, and (iii) the sensitivity of the optimization functional to local spectral features. Parameter points associated with the resonant regime show inconsistent or unstable fits; for this reason we do not include them in the exponent summary. Overall, the extracted exponent ranges are robust across observables and provide a consistent characterization of

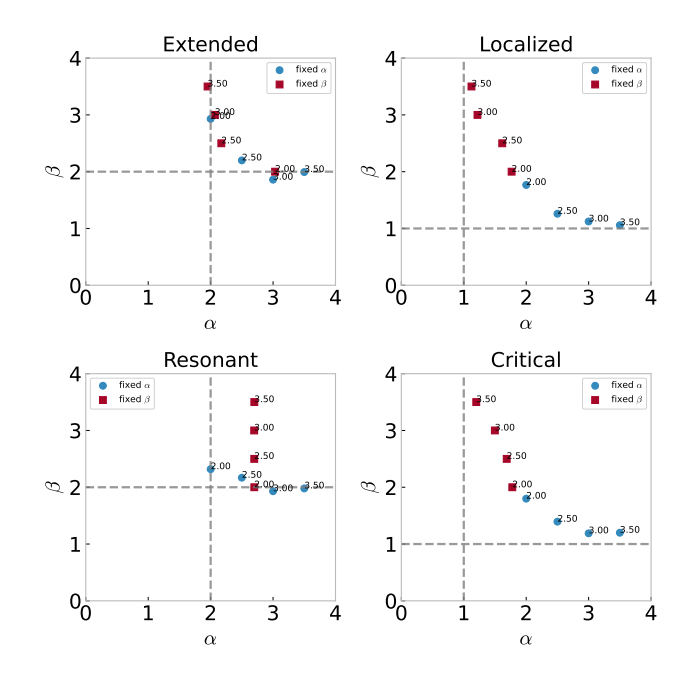


FIG. 7. Critical points in the (α, β) plane extracted from finite-size collapses of the four state-fractions f (extended, localized, resonant, critical). Each marker represents a collapse result at a fixed complementary parameter (labels indicate the fixed value). Different markers denote whether the point was obtained from a fixed- α (circle) or fixed- β (square) sweep.

the critical behaviour in this model.

F. Machine Learning Analysis of the Emergent Phases

To complement our statistical and spectral analyses, we employed machine learning (ML) techniques to investigate whether the phase structure of the system—localized, extended, resonant, and critical—can be inferred directly from the numerical observables without explicit physical input. The objective was twofold: (i) to test if the data possess an intrinsic low-dimensional representation encoding the essential physical organization, and (ii) to assess whether the physically defined quantities f_j (fractions of eigenstates of type j) indeed span the natural manifold of the model. If an unsupervised or weakly supervised algorithm autonomously reconstructs the same latent structure as f_j , this provides strong evidence that the chosen descriptors are physically meaningful rather than arbitrary parametrizations.

We employ a supervised autoencoder (AE) to extract high-level structure from the spectral data. Each eigenstate is represented by a four-component feature vector r, $\rho_{\rm typ}/\rho_{\rm ave}$, ${\rm PR}/N$, and $S_{\rm proxy}$, computed in 40 uniform energy bins within the window $E \in [-2,2]$. The AE consists of an encoder–decoder network with latent dimension $d_z=4$ and a single hidden layer of width 32. Training proceeds in two stages: an unsupervised phase

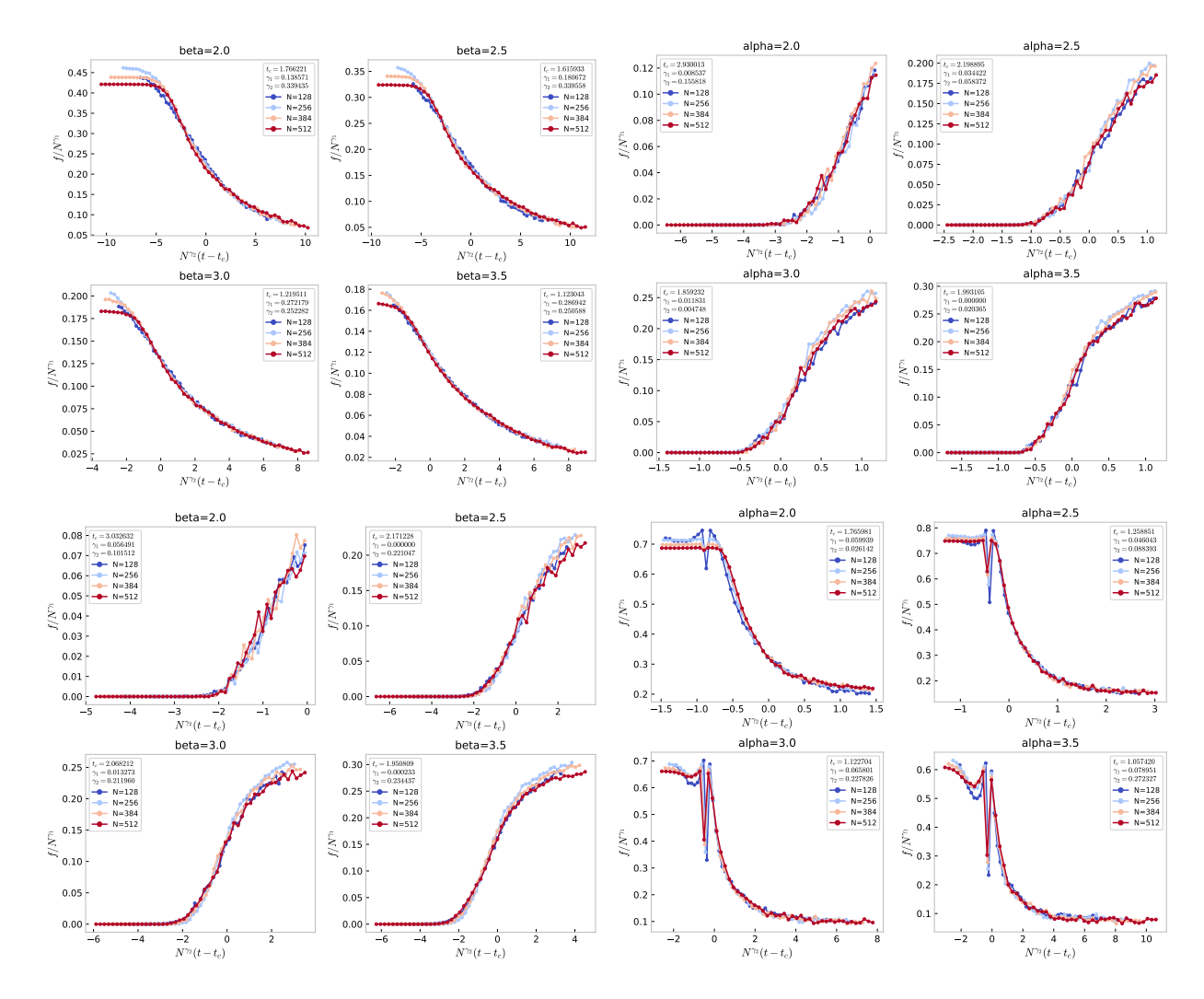


FIG. 8. Representative finite-size collapses. For each panel the inset (legend) reports the optimized parameters $(t_c, \gamma_1, \gamma_2)$. The data shown correspond to system sizes $N = \{128, 256, 384, 512\}$.

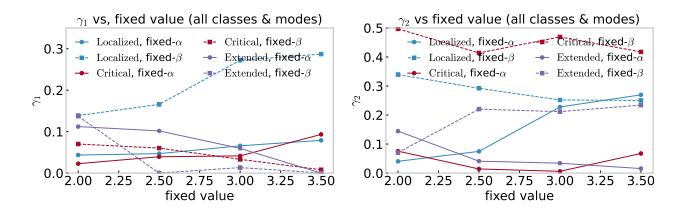


FIG. 9. Extracted critical exponents obtained from the smoothness-based finite-size scaling analysis. Left: Fitted values of γ_1 for all transition lines where a stable collapse is achieved; all data satisfy $\gamma_1 < 0.3$. Right: Corresponding γ_2 values, all lying below $\gamma_2 < 0.5$. Resonant-regime points are omitted due to inconsistent or non-convergent optimization.

minimizing the reconstruction loss, followed by a brief supervised finetuning stage in which a softmax classifier attached to the latent layer is trained against the phase-fraction labels $f_j(\alpha, \beta)$. This light supervision, implemented with early stopping and a mild disentan-

gling penalty ($\beta_{\rm disc} \sim 10^{-2}$), does not impose any explicit correspondence between latent coordinates and the f_j , but sharpens the latent organization such that the four regimes—localized, extended, resonant, and critical—form clearly separated manifolds in the learned representation.

After training, the latent projections $z_i(\alpha,\beta)$ exhibit well-separated regions corresponding to the four known phases. For each latent coordinate, we constructed parameter maps and compared them to the maps of the physical fractions $f_j(\alpha,\beta)$. The correspondence is striking: one-to-one alignment between the z_i -maps and the f_j -maps emerges naturally, even though the network was not instructed to reproduce f_j explicitly. The logistic classifier trained on the latent space achieves high accuracy in predicting the physically defined phases, indicating that the latent embedding faithfully encodes the phase topology of the system.

The convergence between the ML-derived latent variables and the physical phase fractions has direct physical

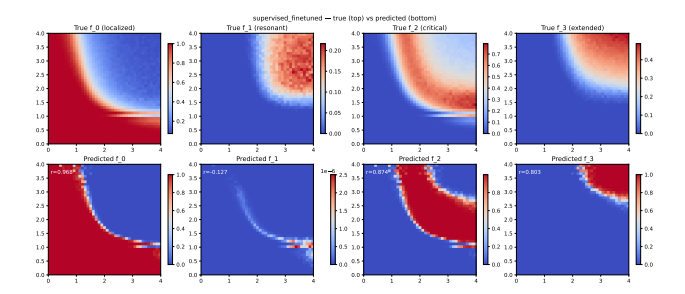


FIG. 10. (Color online) Comparison between the supervised-autoencoder latent coordinates $z_i(\alpha, \beta)$ (top row) and the corresponding physics-based phase fractions $f_j(\alpha, \beta)$ (bottom row). Each column highlights one of the four spectral regimes: localized, extended, resonant, and critical. The latent representation faithfully reproduces the spatial structure of the localized, extended, and critical sectors. For the resonant regime, the correspondence remains approximate: narrow, irregular spectral windows that define the resonant class lead to reduced stability under supervised training, a behaviour consistent with the strong sample-to-sample fluctuations already observed in the physical diagnostics. Overall, the close agreement between z_i and f_j confirms that the autoencoder extracts a latent geometry that mirrors the organization of phases across the (α, β) plane.

significance. First, it confirms that the chosen f_j constitute a faithful parametrization of the true physical manifold governing the localization—delocalization crossover. In other words, the autoencoder—trained without explicit knowledge of the Hamiltonian—discovers the same low-dimensional structure encoded in the theoretically defined f_j . This implies that the statistical features provided to the network inherently contain all necessary physical information, validating that the f_j are not arbitrary constructs but emergent quantities naturally arising from the data.

Second, the success of the supervised AE demonstrates the capability of machine learning as a diagnostic and verification tool in condensed matter physics. Here, ML functions as an independent, data-driven probe: it confirms the phase organization and provides an unbiased mapping of the parameter space. The machine learning analysis serves both as a verification and as a discovery mechanism. This result not only strengthens the validity of the analytical and numerical findings but also highlights the potential of hybrid physics—ML methodologies for identifying order parameters and phase boundaries in complex quantum systems.

V. CONCLUSION AND OUTLOOK

In this work we have carried out a comprehensive investigation of a one-dimensional tight-binding model featuring the simultaneous presence of long-range correlated onsite potentials (controlled by the exponent α)

and algebraically decaying long-range hopping amplitudes (parameterized by β). Using exact diagonalization for system sizes up to N=1024, we combined level statistics, energy-resolved localization measures, phase-characterization functions f_i , finite-size scaling analyses, and machine-learning-based classification to produce a coherent characterization of the phase structure in the (α, β) plane.

Our results demonstrate that the interplay between correlation in the disorder potential and power-law hopping leads to robust mobility edges across significant regions of the phase diagram. Energy-resolved participation ratios, entanglement measures, and the behavior of r-statistics collectively reveal spectral windows in which eigenstates transition as a function of energy.

The four phase-characterization functions f_1 – f_4 , synthesized from complementary diagnostics, provide a compact and operationally effective parameterization of the emergent phases. Finite-size scaling, aided by an explicit smoothness-enforcing cost function, yields consistent estimates for transition points and reveals approximate scaling exponents, though we emphasize that uncertainty remains substantial due to limited accessible system sizes.

A supervised autoencoder was trained on local spectral features, showing that its latent variables faithfully reproduce the structure of the f_i -maps. This agreement provides an independent validation of our physics-driven diagnostics and indicates that the set of handcrafted observables captures the essential phenomenology of the localization transitions.

Beyond the results presented here, several substantive questions remain open. First, the sharp phase boundaries inferred from the f_i maps suggest underlying analytical structures that are not yet understood; developing perturbative or continuum approximations—particularly in the limits of large or small β —may clarify the origin of these transitions. Second, the multifractal properties observed in the mixed and critical regimes warrant deeper analysis, especially regarding how long-range hopping modifies standard multifractal scaling relations. Finally, extending the present framework to interacting systems remains a compelling direction: the combined effects of long-range correlated disorder and algebraic hopping may produce unconventional many-body mobility edges or alter the stability of many-body localization, questions that are presently unresolved.

Overall, our study provides a unified framework to analyze and interpret localization phenomena in long-range, correlated disordered systems and opens up several pathways for future developments in both analytical and numerical fronts.

ACKNOWLEDGMENTS

This work was supported by the Iran National Science Foundation (INSF).

- L. Santos and G. Rigolin, Physical Review A—Atomic, Molecular, and Optical Physics 71, 032321 (2005).
- [2] F. P. Toldin, J. Figgins, S. Kirchner, and D. K. Morr, Physical Review B—Condensed Matter and Materials Physics 88, 081101 (2013).
- [3] M. Walschaers, F. Schlawin, T. Wellens, and A. Buchleitner, Annual Review of Condensed Matter Physics 7, 223 (2016).
- [4] A. Dobrinevski, P. Le Doussal, and K. J. Wiese, Physical Review E—Statistical, Nonlinear, and Soft Matter Physics 83, 061116 (2011).
- [5] U. Mishra, D. Rakshit, R. Prabhu, A. S. De, and U. Sen, New Journal of Physics 18, 083044 (2016).
- [6] P. W. Anderson, Phys. Rev. 109, 1492 (1958).
- [7] E. Abrahams, P. W. Anderson, D. C. Licciardello, and T. V. Ramakrishnan, Phys. Rev. Lett. 42, 673 (1979).
- [8] F. A. B. F. de Moura and M. L. Lyra, Phys. Rev. Lett. 81, 3735 (1998).
- [9] F. Izrailev and A. Krokhin, Physical review letters 82, 4062 (1999).
- [10] L. S. Levitov, Annals of Physics 8, 697 (1990).
- [11] A. D. Mirlin and Y. V. Fyodorov, Phys. Rev. Lett. 76, 116 (1996).
- [12] A. D. Mirlin, Y. V. Fyodorov, F.-M. Dittes, J. Quezada, and T. H. Seligman, Physical Review E 54, 3221 (1996).
- [13] B. Pérez-González, M. Bello, Á. Gómez-León, and G. Platero, Physical Review B 99, 035146 (2019).
- [14] G. Celardo, R. Kaiser, and F. Borgonovi, Physical Review B 94, 144206 (2016).
- [15] L. Levitov, Annalen der Physik **511**, 697 (1999).
- [16] S. Nag and A. Garg, Physical Review B 99, 224203 (2019).
- [17] R. Singh, R. Moessner, and D. Roy, Physical Review B 95, 094205 (2017).
- [18] C. Zhou and R. Bhatt, Physical Review B 68, 045101 (2003).

- [19] L. Qi, Y. Yan, Y. Xing, X.-D. Zhao, S. Liu, W.-X. Cui, X. Han, S. Zhang, and H.-F. Wang, Physical Review Research 3, 023037 (2021).
- [20] S.-S. Wang, K. Li, Y.-M. Dai, H.-H. Wang, Y.-C. Zhang, and Y.-Y. Zhang, Scientific Reports 13, 5763 (2023).
- [21] D. A. Keen and A. L. Goodwin, Nature **521**, 303 (2015).
- [22] P. Carpena, P. Bernaola-Galván, P. C. Ivanov, and H. E. Stanley, Nature 418, 955 (2002).
- [23] V. D. Neverov, A. E. Lukyanov, A. V. Krasavin, A. Vagov, and M. D. Croitoru, Communications Physics 5, 177 (2022).
- [24] Q. Li, E. H. Hwang, E. Rossi, and S. Das Sarma, Phys. Rev. Lett. 107, 156601 (2011).
- [25] M. Pouranvari and H. M. Moghaddam, Physica Scripta 100, 055935 (2025).
- [26] N. Defenu, T. Donner, T. Macrì, G. Pagano, S. Ruffo, and A. Trombettoni, Reviews of Modern Physics 93, 025001 (2021).
- [27] U. Kuhl, F. Izrailev, A. Krokhin, and H.-J. Stöckmann, Applied Physics Letters 77, 633 (2000).
- [28] N. C. Chávez, F. Mattiotti, J. Méndez-Bermúdez, F. Borgonovi, and G. L. Celardo, Physical Review Letters 126, 153201 (2021).
- [29] M. Bixon, B. Giese, S. Wessely, T. Langenbacher, M. E. Michel-Beyerle, and J. Jortner, Proceedings of the National Academy of Sciences 96, 11713 (1999).
- [30] F. Ito, T. Ikoma, K. Akiyama, Y. Kobori, and S. Tero-Kubota, Journal of the American Chemical Society 125, 4722 (2003).
- [31] S. Aubry and G. André, Ann. Israel Phys. Soc 3, 18 (1980).
- [32] S. Sarkar, B. K. Agarwalla, and D. S. Bhakuni, Phys. Rev. B 109, 165408 (2024).
- [33] V. Oganesyan and D. A. Huse, Phys. Rev. B 75, 155111 (2007).